Square-Wave Drive for Synchronous Reluctance Machine and its Torque Ripple Analysis

Jian-Xin Shen, Shun Cai, Dong-Min Miao, Dan Shi, Jacek Gieras, and Yun-Chong Wang

***Abstract*—Synchronous reluctance machine (SynRM) can be perceived as a special type of permanent magnet synchronous machine (PMSM), and shares similar control method, i.e. the sine-wave current drive with sinusoidal phase currents. In this paper, square-wave drive, which is employed for permanent magnet brushless (BLDC) motors, is employed for the SynRM, in order to economically reduce the cost of rotor position sensor. It is revealed that the torque density and efficiency are slightly sacrificed, whereas torque ripple is deteriorated, proving the SynRM with square-wave drive still promising for the cost-sensitive application if torque ripple is not considered as a critical issue. To further investigate the additional pulsating torque under square-wave drive, mathematical model based on a-b-c phase inductance and d-q axis inductance are established, together with the time-stepping FE calculated currents. It is concluded that the harmonics in the currents tend to cause non-sinusoidal variation of the magnetic reluctance, which can be represented as additional inductance harmonics. The harmonics of the current and inductance interact with each other, thus undesirable torque ripple components are produced.**

***Index Terms*— Synchronous reluctance machine, pulsating torque, square-wave drive, inductance, magnetic saturation.**

I. INTRODUCTION

SYNCHRONOUS reluctance machine (SynRM) can be perceived as an exceptional type of PMSM, in which flux linkage of magnet is zero (for the pure SynRM) or rather low (for the permanent magnet (PM) assisted SynRM), whereas the rotor is salient with different magnetic reluctance in direct-axis (*d*-axis) and quadrature-axis (*q*-axis) [1] [2]. Consequently, the typical control strategy for the SynRM is identical with PMSM with a sinusoidal phase current injected along the armature winding which is thus denoted as sine-wave drive, [3] [4]. Numerous investigations have been conducted to illustrate the potential substitution of the SynRM for conventional PMSM and inductance machine in cost-effective industrial applications [5] [6]. However, to achieve sine-wave drive, a high-resolution rotor position sensor as well as complex controller are required, hence, the system cost is high, restricting the utilization for cost-effective applications. To further reduce the hardware cost and simplify the control strategies, the square-wave drive with a lower resolution position sensor is adopted for the SynRM in [7]. Hereby, the square-wave drive is the one which has been widely used for PM brushless DC (BLDC) motors, in which square-wave voltages are applied to the machine armature windings.

For the square-wave drive, abundant time harmonics are introduced in the armature current, and the additional current harmonics tend to deteriorate the torque performance. Firstly, the current harmonics deteriorate the air-gap flux density, thus, local saturation may be caused. It has been demonstrated in [8] that magnetic saturation has a detrimental effect on the rotor saliency, and consequently, the average torque can be reduced. Besides, the torque ripple of the SynRM is strongly dependent on the armature winding magnetomotive force (MMF) harmonics [9] [10]. The magnetic reluctance as well as inductance can be varied at different positions due to the current harmonics caused local magnetic saturation. As a result, additional pulsating torque is produced and the torque waveform is deteriorated.

It has been widely investigated that the torque ripple in the SynRM is large if not designed properly [11]. Some design techniques have been conducted to mitigate the fluctuating torque for the SynRM to obtain smooth operation in [12]-[19]. In [12] and [13], the rotor flux barrier is regarded as slots in rotor, and the combination of stator slots per pole pair and rotor slots per pole pair is optimized to achieve low torque ripple. To reduce the reluctance discontinuity, the end of rotor barrier has been notched to ensure the flux lines entering the rotor smoothly [14]. Moreover, a 'Machaon' rotor is proposed in [15] by employing different flux barrier end angles for adjacent flux barriers, and a rotor composed of 'Romeo' part and 'Juliet' part is proposed in [16] to compensate the torque pulsating components. Besides, a rotor structure with asymmetric flux barrier is presented in [17][18][19], for example, by shifting the center line of each flux barrier at a stator slot pitch to compensate the torque ripple caused by the stator slot harmonics. To avoid the unbalance of rotor structure, [18] proposes an asymmetric flux barrier rotor structure by shifting

Manuscript received October 19, 2021; revised November 22, 2021; accepted December 03, 2021. date of publication December 25, 2021; date of current version December 18, 2021.

This work was supported in part by the National Natural Science Foundation of China under Grant 52007161.(*Corresponding Author: Shun Cai*)

J. X. Shen, D. M. Miao, D. Shi, Y. C. Wang are with the College of Electrical Engineering, Zhejiang University, Zhejiang Provincial Key Laboratory of Electrical Machine Systems, Hangzhou, 310027, China. (e-mail: J_X_Shen@zju.edu.cn, miaodongmin@zju.edu.cn, shidan1108@zju.edu.cn, wangycee@zju.edu.cn)

S. Cai is with the School of Electrical and Electronic Engineering, Nanyang Technological University, 639798, Singapore. (e-mail: shun.cai@ntu.edu.sg)

J. Gieras is with the Department of Electrical Engineering, UTP University of Science and Technology, Bydgoszcz, 85-796, Poland. (e-mail: jacek.gieras@utp.edu.pl)

Digital Object Identifier 10.30941/CESTEMS.2021.00032

the flux barrier end merely. To achieve low torque ripple in dual directions, two asymmetric rotor laminations are combined axially. In [20], a SynRM prototype with torque ripple less than 2% is achieved, by selecting fractional-slot distributed winding and optimizing the flux barrier end.

Although there are some publications comparing the sine-wave drive and square-wave drive for PM machines [21] [22], the performance of SynRM with square-wave drive has hardly been investigated [7]. Additional low-cost PM can be attached at an end of rotor to facilitate the Hall-effect sensors for the SynRM with square-wave drive, which helps reduce the cost of the rotor position sensor. Moreover, to the author's knowledge, all the published techniques to reduce the SynRM torque ripple are based on sinusoidal currents, which means that the effect of time harmonics in the armature currents has not been examined in detail. Therefore, this paper tries to fill this gap and discusses about the pulsating torque component of the SynRM with square-wave drive, for which the prototype discussed in [20] is used, as shown in Fig. 1.

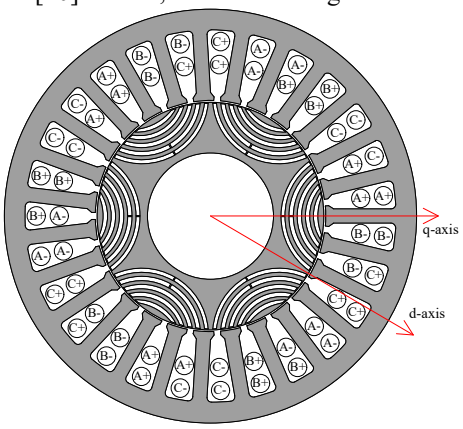

Fig. 1. Topology of the investigated SynRM.

This paper will be organized as follows. Firstly, the cross-section and main parameters of the investigated SynRM will be presented. The optimized machine exhibits significant difference between *d*-*q* axis inductances, and the reluctance torque is produced based on the saliency. Furthermore, the electromagnetic performance with sine-wave and square-wave drives are compared comprehensively to demonstrate the feasibility and potential application. Finally, analytical torque model is established based on the interaction of inductance and current, in order to analyze the origination of the torque pulsation component in the SynRM with square-wave drive.

II. Synchronous Reluctance Machine

The SynRM investigated in this paper is presented in Fig. 1, with the design parameters listed in Table I. A multi-layer flux barrier rotor is adopted for the SynRM to boost the rotor saliency and reluctance torque. A fractional slot distributed winding is employed to suppress the torque ripple for smooth operation. Two iron bridges are designed in the inner center flux barrier to ensure the mechanical stress at maximum speed operation. This machine has been optimized for maximum torque density and minimum torque ripple with sinusoidal-wave drive in [19], where the torque ripple is defined as the ratio of peak-peak torque to average torque in this paper.

At rated current amplitude excitation, the flux line distribution with current vector along *d*- and *q*-axes are compared in Figs. 2 (a) and (b), respectively. As can be observed, the flux lines pass through rotor iron segment with *d*-axis current, whereas the flux lines are blocked by the rotor flux barrier with *q*-axis current. Fig. 3 shows the winding flux linkage with armature current applied with different angles. The winding flux linkage is maximized with armature current along *d*-axis and minimized with current along *q*-axis, regardless of current amplitude.

TABLE I
Design Parameters of The SynRM

Parameter	Value	Parameter	Value
Rated power, kW	5	Rated speed, rpm	3000
Pole-pair number	3	Stator slot number	27
Air-gap length, mm	0.8	Stack length, mm	75
Stator outer radius, mm	90.5	Rotor flux barrier number	5
D-axis inductance, mH	19.5	Q-axis inductance, mH	6.2
Rated current, A_{rms}	18.4	Phase resistance, ohm	0.2

As a result, the magnetic reluctance is larger in *q*-axis with the multi-layer flux barrier design and the inductance difference between *d*-axis and *q*-axis is produced. At rated working point, the saliency ratio of the investigated SynRM is around 3.1, with *d*-axis inductance of 19.5mH and *q*-axis inductance of 6.2mH.

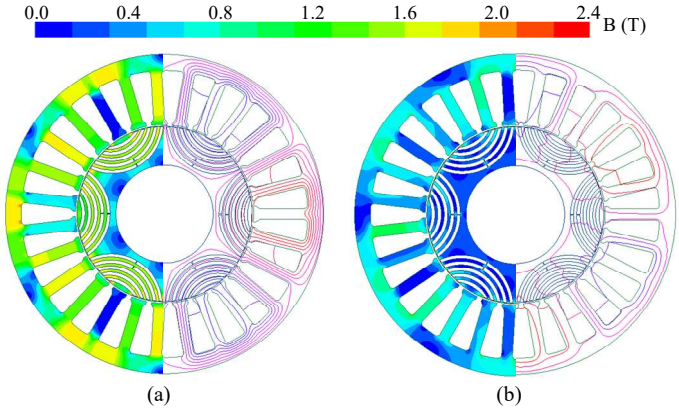

Fig. 2. Flux line and magnetic field distribution under rated current excitation. (a) Armature current applied along *d*-axis. (b) Armature current applied along *q*-axis.

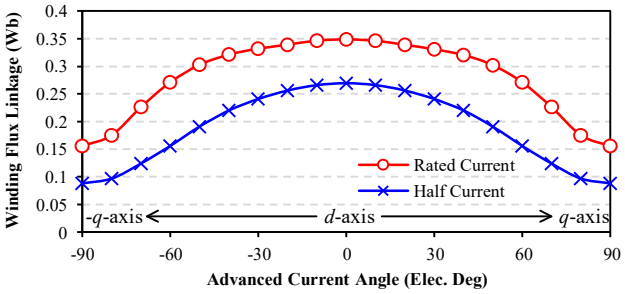

Fig. 3. Armature flux linkage variation with advanced current angle under constant input current amplitude.

III. Comparative Analysis with Sine-Wave and Square-Wave Drives

Hardware for both sine-wave and square-wave drives is

similar, except that the sine-wave drive needs a high-resolution rotor position sensor (e.g., encoder or resolver) to detect the current angle at all times, whilst the square-wave drive requires low resolution sensors (e.g., Hall-effect sensors) to determine the switch on and off for the six power devices in the drive circuit. Although there exist no PM in the rotor of the pure SynRM, additional PM can be attached at the end of rotor to facilitate the Hall-effect sensors. Subsequently, the square-wave drive hardware is still cheaper and is promising for the SynRM, making it more attractive for cost sensitive applications.

A. *Sine-Wave Drive*

For the sine-wave drive, the current time harmonics can be neglected supposing the DC voltage and the PWM switching frequency are sufficient. To simplify the analysis, an ideally sinusoidal current without time harmonics is considered for the sine-wave drive in following discussion.

The *d*-axis inductance and *q*-axis inductance variations with the corresponding currents are shown in Fig. 4, where the current is normalized by the rated current, using the per-unit value. The *d*-axis inductance varies with the *d*-axis current since the armature current tends to saturate the iron segment and increases the reluctance. When the current amplitude is small, the rotor flux bridges are not saturated, hence the *q*-axis inductance is relatively large. With the increase of currents, the rotor flux bridges become more and more saturated, the *q*-axis inductance is then reduced and hardly varies with the current, therefore, the rotor saliency is produced. To conclude, the rotor saliency is determined by the armature current, and a proper current angle should be determined to obtain significant reluctance torque.

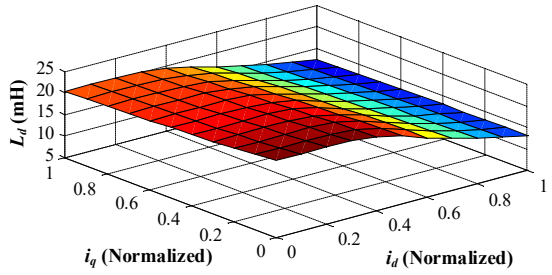

(a)

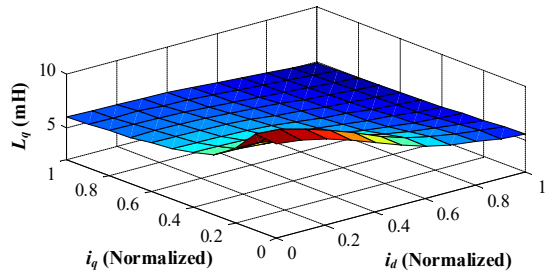

(b)

Fig. 4. Inductances variation with armature currents. (a) *d*-axis inductance. (b) *q*-axis inductance.

Fig. 5 shows the average torque versus the amplitude of armature current and advanced current angle, under the calculation of 2-dimensional finite element simulation (2D-FEM). The armature current amplitude is normalized by the rated value in Table I, and the advanced current angle is defined as the angle by which the armature current vector leads the *d*-axis. The average torques are zero when the armature current is applied either along *d*-axis or *q*-axis, e.g. phase angle of 0°or 90°. When the armature current is applied between *d*- and *q*-axes, the reluctance torque is produced based on the difference between *d*- and *q*-axis inductances. The optimal current angle to obtain maximum torque per ampere (MTPA) control is further denoted with bold line.

When the current amplitude is small, the iron core is not saturated and the current phase to obtain MTPA control is around 45°. When the machine is working under heavy load with relatively large armature current, the magnetic saturation becomes significant. In that condition, the armature current vector moves towards the *q*-axis since the *d*-axis inductance is more sensitive with the armature current, see Fig. 4. As a result, the optimal advanced current angle increases with the armature current amplitude gradually. Under the rated working condition, the optimal armature current angle with MTPA control is around 57°.

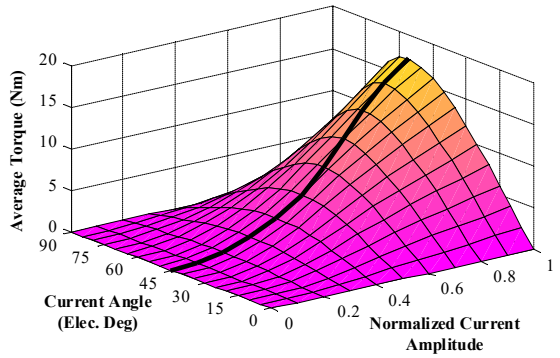

Fig. 5. Variation of electromagnetic torque with stator current amplitude and phase angle.

According to the torque variation with current amplitude and phase angle in Fig. 5, the electromagnetic torque of the SynRM is calculated with 2D-FEA, and Fig. 6 shows the torque waveforms under different current amplitudes for the MTPA control. Overall, the electromagnetic torque waveforms are smooth since the machine has been optimized for minimum torque ripple under ideally sinusoidal armature current. With rated armature current, the pulsating torque is negligible and the torque ripple is as low as 2%, with average value of 17.2 Nm.

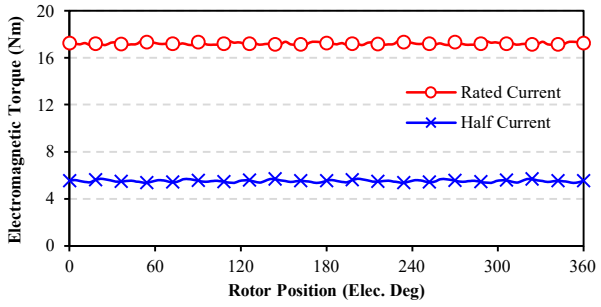

Fig. 6. Output torque waveform with sine-wave drive.

B. *Square-Wave Drive*

To simplify the control strategy and reduce the hardware cost for economical industrial application, this paper further evaluates the electromagnetic performance of the SynRM with square-wave drive in substitution for the sine-wave drive, similar with the BLDC drive for permanent magnet machine. Ideally, a rectangular current is applied to the winding by controlling the switch on and off time for the power devices in the inverter. The supplied voltage and current are further regulated by the duty ratio of the PWM signal. Fig. 7 shows the theoretical current waveforms with sine/square wave drives. By controlling the turning on and off time for the power devices, the advanced current angle for the square-wave drive can be regulated. Theoretically, the armature current should be applied ahead of *d*-axis with electrical angle of 45°, identical to that in the sine-wave drive.

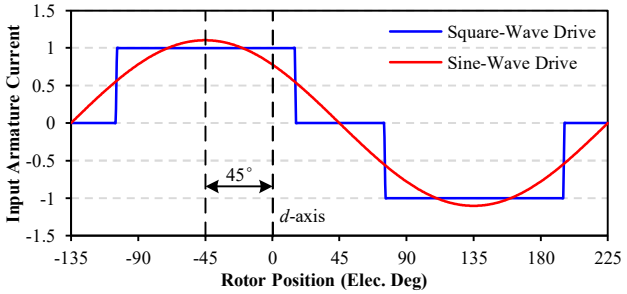

Fig. 7. Theoretical armature current comparison with sine/square wave drives.

Nevertheless, square-wave voltage is supplied to the armature winding, instead of square-wave current for the practical control, which is similar with that in PM BLDC drive. Due to the large inductance in the SynRM, the armature current falls behind the voltage and the current waveform is rectified with less harmonics compared with the voltage square waveform. Supposing the switches are controlled according to the time sequence in Fig. 7, the practical armature current phase will be retarded significantly than the theoretical value. To obtain maximum output capability for the square-wave drive, the switches of the inverter should be controlled with an advanced angle. With the utilization of field-circuit coupling simulation, the optimal advanced current angle for square-wave drive to obtain MTPA control can be obtained.

At the MTPA control point, the phase current under square-wave drive is shown in Fig. 8, in comparison with the sine-wave drive. As can be seen, although square-wave control is employed, the phase current waveform is quite sinusoidal due to the inherently large self inductance in the SynRM. Additional harmonics, e.g., 5th and 7th, are introduced in the square-wave drive compared with the ideally sine-wave drive. Under the same root-mean-square in one period with the sine-wave current, the fundamental of the square-wave drive is reduced due to the increased harmonics. Moreover, the angle between fundamental armature current with *d*-axis is around 65°, and slightly larger than that with the sine-wave drive (57°). Although additional harmonics are inevitably introduced in the current of square-wave drive with simpler control strategy, the current harmonics are of small amplitude and the waveform is quite sinusoidal.

Furthermore, electromagnetic torque waveforms under full and half of the rated current with the square-wave drive are shown in Fig. 9. Although the current harmonics are not abundant in the armature current with square-wave drive, as shown in Fig. 8, the electromagnetic torque waveform is deteriorated significantly. As can be observed from Fig. 9, the pulsating torque is significant with square-wave drive, and the torque ripple is around 40%, with average value of 16.4Nm. The reason accounting for the significant torque ripple will be further investigated in section IV.

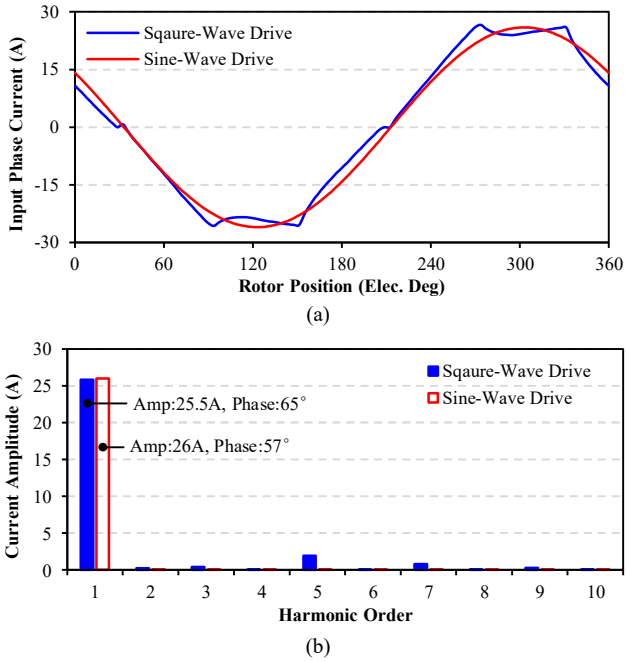

Fig. 8. Practical armature current with optimal advanced current angle for MTPA control. (a) Waveform. (b) Spectrum.

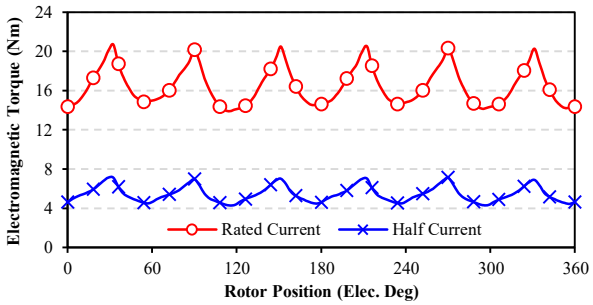

Fig. 9. Electromagnetic torque waveform with square-wave drive.

C. *Performance Comparison*

Based on the above analysis, the average torque and torque ripple under different current amplitudes with sine-wave and square-wave drives are compared in Fig. 10. With the same RMS value of input stator current, the average torque of the square-wave drive is just slightly lower than that of sine-wave drive, less than 5%. However, the torque ripple is increased significantly under square-wave drive. With ideal sine-wave current excitation, the torque ripple is lower than 10% under twice rated current. However, the torque ripple is deteriorated significantly with square-wave drive. The enlarged torque ripple is observed at light load, and the increased ratio is maximized approaching rated current. The pulsating torque ratio can be higher than 30% with square-wave drive, which

tends to cause vibration and noise.

On the other hand, the on-load line-line voltages of the sine-wave drive and square-wave drive at the rated speed are shown in Fig. 11, which reflects the requirement of inverter and power supply volume. With sine-wave drive, both the voltage and current waveforms are sinusoidal with accurate real-time rotor position detection. With square-wave drive, the voltage waveform tends to be square by controlling the switch on and off at several typical positions. At each typical position with switch on and off, there is spark in the voltage due to the sudden change of current. Although the phase voltage of the sine-wave drive is more sinusoidal, the maximum values of both drives are approximately the same. Therefore, the demand for the inverter and DC bus voltage is nearly unchanged by replacing the sine-wave drive with the square-wave drive.

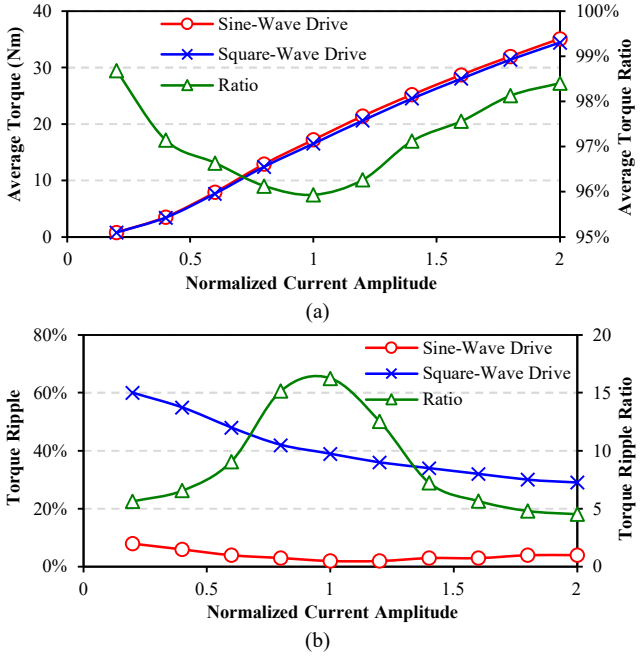

Fig. 10. Comparison of torque characteristics with sine-wave and square-wave drives. (a) Average torque. (b) Torque ripple.

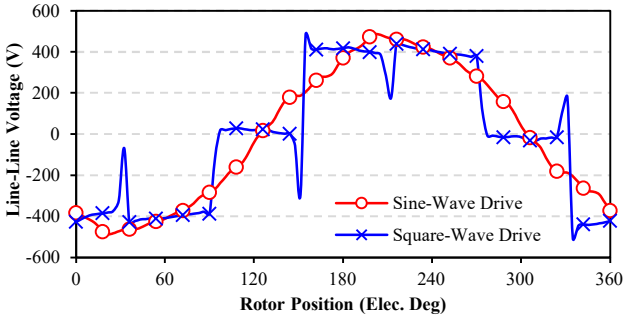

Fig. 11. On-load line-line voltage comparison of sine-wave drive and square-wave drives under rated current with MTPA control.

Furthermore, the machine efficiency under rated current along different speeds with two different control strategies is compared in Fig. 12. The copper loss is constant under the same RMS value of armature current for sine-wave and square-wave drives. The iron loss is obviously higher in the square-wave drive due to more abundant current and field harmonics. Due to the lower torque density and higher iron loss, the motor efficiency with square-wave drive is lower than that with sine-wave drive. Moreover, the efficiency reduction is more obvious at high speed, due to dominant iron loss with higher frequency. At rated speed of 3000 rpm, the efficiency is reduced to ~0.5% with the utilization of square-wave drive.

Based on the above analysis, the main performance comparisons for the SynRM with the sine-wave drive and square-wave drive are summarized in Table II. With non-rare earth PM design, the material cost of the SynRM prototype is relatively low, which is attractive for cost-sensitive application. With sine-wave drive, the encoder or resolver is required to detect rotor position and the sensor cost can be higher than the prototype. For contrast, the cost of rotor position sensor can be reduced significantly with square-wave drive. Furthermore, the amplitude of the phase voltage is hardly increased and the torque density is reduced less than 5% with the substitution of square-wave drive for the original sine-wave drive. The performances with square-wave drive are not really deteriorated, except the significant torque ripple. Therefore, the square-wave SynRM drive is still acceptable for low-cost applications, in which the torque ripple is not critically concerned.

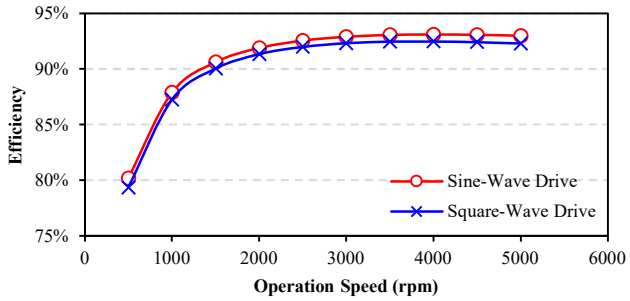

Fig. 12. Machine efficiency versus operation speed comparison under rated current excitation.

TABLE II
*PERFORMANCE COMPARISON WITH SINE-WAVE AND SQUARE-WAVE DRIVES FOR SYNRM

Performance	Sine-Wave Drive	Square-Wave Drive
Machine material cost	~42USD	
Position sensor	Encoder or resolver	Hall-effect sensor
Sensor volume	Large	Small
Sensor cost	>40USD	~1USD
Phase current RMS	18.4A	
Current angle (fundamental)	57°	65°
Phase current THD	0 (Ideal)	7.9%
Average torque	17.2Nm	16.4Nm
Torque ripple	2%	40%
Line-line peak voltage	487V	495V
Efficiency	92.8%	92.3%

*Performance evaluated under rated speed and current with MTPA control

IV. TORQUE RIPPLE ANALYSIS

It can be observed that the current waveform with square-wave drive is not severely deteriorated, whereas the torque ripple is increased significantly. In this section, the origination of the additional pulsating torque component in the square-wave SynRM drive will be investigated based on mathematical models.

A. Stationary A-B-C Phase Inductance Model

Firstly, the three-phase armature current with the consideration of time harmonics in the stationary frame can be

expressed as follow

$$\mathbf{I}_{\mathbf{abc}}=\begin{bmatrix} i_a \\ i_b \\ i_c \end{bmatrix}=\sum_{j=6i+1}\begin{bmatrix} I_j\cos\left(j\theta_e+\beta_j\right) \\ I_j\cos\left[j\left(\theta_e-\tfrac{2}{3}\pi\right)+\beta_j\right] \\ I_j\cos\left[j\left(\theta_e+\tfrac{2}{3}\pi\right)+\beta_j\right] \end{bmatrix} \tag{1}$$

where I_j and β_j represent the amplitude and electrical angle of the jth order harmonic in the armature current, respectively, and θ_e is the relative rotating electrical angle.

For the ideal sine-wave drive, only the fundamental is considered for the armature current, viz. j=1. For the square-wave drive, additional harmonics are introduced in the armature current, such as j=-5 and j=7, see Fig. 8. The harmonic order with negative value denotes that the rotating direction of certain harmonic field is opposed to the rotor rotating direction.

Furthermore, the self and mutual inductances of three-phase armature winding with the consideration of harmonics can be decomposed with Fourier series in Eqs.(2) and (3), where α_k is the electrical phase shift for certain order harmonic of inductance due to magnetic saturation [23].

$$\mathbf{L}_{\mathbf{abc}}=\begin{bmatrix} L_{aa} & M_{ab} & M_{ac} \\ M_{ba} & L_{bb} & M_{bc} \\ M_{ca} & M_{cb} & L_{cc} \end{bmatrix} \tag{2}$$

$$\begin{cases} L_{aa}=\sum\limits_{k=0,2,4\cdots}L_k\cos\left(k\theta_e+\alpha_k\right) \\ L_{bb}=\sum\limits_{k=0,2,4\cdots}L_k\cos\left[k\left(\theta_e-\tfrac{2}{3}\pi\right)+\alpha_k\right] \\ L_{cc}=\sum\limits_{k=0,2,4\cdots}L_k\cos\left[k\left(\theta_e+\tfrac{2}{3}\pi\right)+\alpha_k\right] \\ M_{ab}=M_{ba}=\sum\limits_{k=0,2,4\cdots}M_k\cos\left[k\left(\theta_e+\tfrac{2}{3}\pi\right)+\alpha_k\right] \\ M_{bc}=M_{cb}=\sum\limits_{k=0,2,4\cdots}M_k\cos\left(k\theta_e+\alpha_k\right) \\ M_{ca}=M_{ac}=\sum\limits_{k=0,2,4\cdots}M_k\cos\left[k\left(\theta_e-\tfrac{2}{3}\pi\right)+\alpha_k\right] \end{cases} \tag{3}$$

With the injection of three-phase current, the co-energy stored in the armature winding can be expressed as

$$W_{co}=\frac{1}{2}\mathbf{I}_{\mathbf{abc}}{}^T\mathbf{L}_{\mathbf{abc}}\mathbf{I}_{\mathbf{abc}} \tag{4}$$

Based on the energy variation at different rotor positions, the electromagnetic torque can be calculated from

$$T_e=\frac{\partial W_{co}}{\partial\theta_m}\Big|_{i=constant} \tag{5}$$

where θ_m denotes the rotor mechanical position. The relationship between mechanical position and electrical position is shown in (6), and p is the number of pole-pairs.

$$\theta_e=p\theta_m \tag{6}$$

By solving Eqs.(1)~(6), the electromagnetic torque of the SynRM can be obtained as Eq.(7), where the k_{T1}, k_{T2}, k_{T3}, k_{T4} are corresponding torque coefficients and expressed in Eq.(8).

$$T_e=\sum_{j_1=6i_1+1}\sum_{j_2=6i_2+1}\sum_{k=0,2,4\cdots}-\frac{pkI_{j_1}I_{j_2}}{8}\times \left[\left(k_{T1}+k_{T4}\right)\left(L_k+2M_k\right)+\left(k_{T2}+k_{T3}\right)\left(L_k-M_k\right)\right] \tag{7}$$

$$\begin{cases} k_{T1}=\sum\limits_{\varepsilon=-1,0,1}\sin\left[\left(k+j_1+j_2\right)\theta_e+\beta_{j_1}+\beta_{j_2}+k\alpha_k-\tfrac{2}{3}\left(k-1\right)\varepsilon\pi\right] \\ k_{T2}=\sum\limits_{\varepsilon=-1,0,1}\sin\left[\left(k+j_1-j_2\right)\theta_e+\beta_{j_1}-\beta_{j_2}+k\alpha_k-\tfrac{2}{3}k\varepsilon\pi\right] \\ k_{T3}=\sum\limits_{\varepsilon=-1,0,1}\sin\left[\left(k-j_1+j_2\right)\theta_e-\beta_{j_1}+\beta_{j_2}+k\alpha_k-\tfrac{2}{3}k\varepsilon\pi\right] \\ k_{T4}=\sum\limits_{\varepsilon=-1,0,1}\sin\left[\left(k-j_1-j_2\right)\theta_e-\beta_{j_1}-\beta_{j_2}+k\alpha_k-\tfrac{2}{3}\left(k+1\right)\varepsilon\pi\right] \end{cases} \tag{8}$$

As can be seen from Eq.(7), the effective torque in the SynRM is proportional to the winding inductance and square of armature current. Besides, the instantaneous torque is zero when the self inductance order k=0, indicating the biased value in the phase inductance does not contribute to effective torque. Furthermore, it can be concluded from (8) that the torque coefficient k_{T1} is not zero only when the harmonic order of the phase inductance satisfies k=3m+1, the torque coefficients k_{T2} and k_{T3} are not zero only when k=3m, and the torque coefficient k_{T4} is not zero only when k=3m-1, where m is any integer.

The phase current waveforms and spectra under sine-wave and square-wave drives have been illustrated in Fig. 8. With the frozen permeability calculation in 2D-FEM, the phase self and mutual inductances at corresponding current excitations are calculated and shown in Fig. 13. Obviously, the harmonics in the phase inductance under square-wave drive are more abundant under square-wave drive.

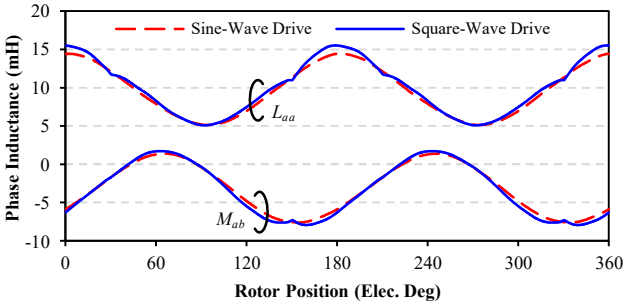

(a)

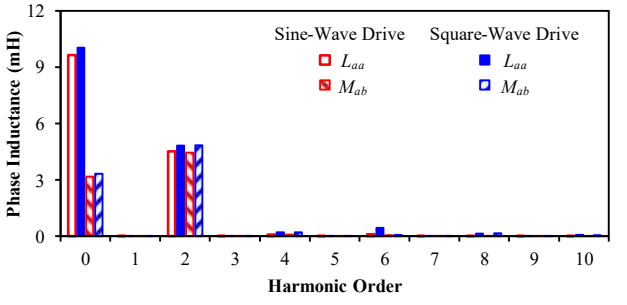

(b)

Fig. 13. Phase inductance obtained from frozen permeability with sine-wave and square-wave drives. (a) Waveforms. (b) Spectra.

For the ideally sine-wave drive, only the fundamental of armature current is considered, viz. j_1=j_2=1 in (8). The inductance waveforms under sine-wave drive are almost sinusoidal, mainly containing the k=0 and k=2 harmonics only

in Fig. 13. In this case, only k_{T4} are not zero in Eq.(8), whereas k_{T1}, k_{T2} and k_{T3} are zero and do not contribute to the instantaneous torque. As a result, the effective torque can be produced only with the interaction of armature current fundamental value with the phase inductance harmonic order of 2, i.e., k=2, j_1=1, j_2=1 in Eq.(8). To conclude, the average reluctance torque of the SynRM considering ideally sine-wave armature current excitation and sine-wave inductance with negligible harmonics can be simplified as Eq.(9). By applying the current and inductance values into Eq.(9), the average torque is calculated as 17.5 Nm, very close to the FEA result (17.2 Nm).

$$T_{sin} = \frac{3}{4} p\left(L_2 + 2M_2\right) I_m^{\,2} \sin\left(2\beta_1\right) \tag{9}$$

For the square-wave drive, the harmonics in the phase current mainly consist of j_1, j_2=1, -5, 7, see Fig. 8. The current harmonics tend to cause local magnetic saturation and magnetic reluctance pulsation. Therefore, additional harmonics are introduced in the phase inductance with square-wave drive, e.g., k=4, 6, 8… in Fig. 13. The increased harmonics in the armature current and inductance interaction with each other, and additional pulsating torque component is produced. By substituting the current and inductance Fourier series into (7), the torque components contributed by current and inductance under stationary frame are summarized in Table III, where j_1 and j_2 are the current harmonic orders, and k is the inductance harmonic order. The torque components with amplitude higher than 1.0 Nm are marked in bold.

It can be observed from Table III that the main torque components include the average torque with zero order and pulsating torque with 6th order under square-wave drive, in consistent with the 2D-FEM results in Fig. 9. The average value originates from the interaction between the armature current fundamental and the 2nd order harmonic in the phase inductances. Meanwhile, the pulsating torque with 6th order harmonic mainly has two resources. The former one is the interaction between the additional current harmonics, e.g., 5th and 7th, with the 2nd order harmonic in the phase inductances. The other is the interaction between the armature current fundamental with the higher order harmonics in the phase inductances, e.g., 4th, 6th and 8th. The high order harmonics in the phase inductance can be reduced with the various design techniques, which is generally adopted in the torque ripple mitigation of SynRM with sine-wave drive [12]-[19]. For the investigated SynRM, the harmonics in the phase inductance are inherently small after parametric optimization, and the torque ripple is negligible with sine-wave current. However, current time harmonics tend to cause local magnetic saturation at different rotor positions and the harmonics in the phase inductance are enlarged with square-wave drive. As a result, although the harmonics in the armature current are small with square-wave drive, the torque ripple is deteriorated significantly.

B. Rotating D-Q Axis Inductance Model

To further illustrate this phenomenon, the electromagnetic torque is calculated in the rotor rotating frame. By transforming the three-phase armature current of Eq.(1) into rotating frame, the input current can be expressed in Eq.(10) and shown in Fig. 14. The fundamental component of the three-phase armature currents has been transformed into the constant value (ν=0th) in the d-q frame, whilst the harmonics with order of j=-5 and j=7 in the square-wave drive are transformed into the ν=6th order harmonic current in the d-q frame. As a result, the d-q axis currents are constant under ideal sine-wave drive and 6th order harmonics are introduced in the d-q axis currents for square-wave drive.

$$\mathbf{I}_{\mathbf{dq}} = \begin{bmatrix} i_d \\ i_q \end{bmatrix} = \sum_{\nu=6i} \begin{bmatrix} I_\nu \cos\left(\nu\theta_e + \beta_\nu\right) \\ I_\nu \sin\left(\nu\theta_e + \beta_\nu\right) \end{bmatrix} \tag{10}$$

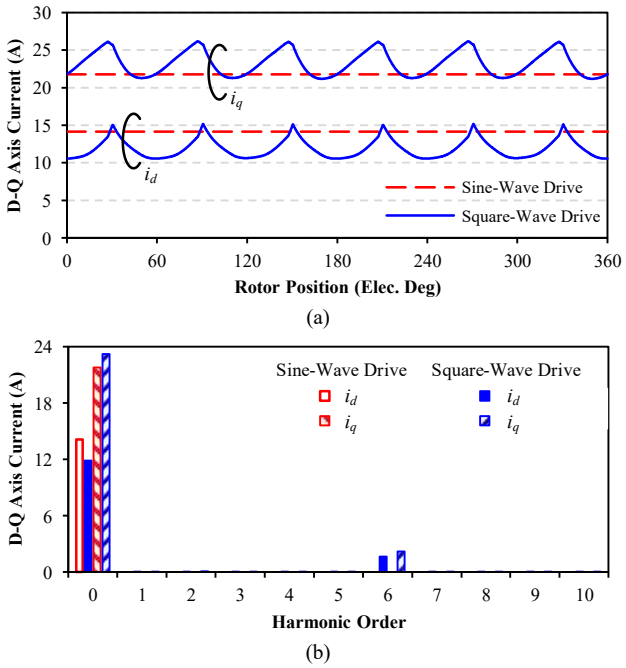

Fig. 14. d-q axis currents with sine-wave and square-wave drives. (a) Waveforms. (b) Spectra.

Considering core saturation and cross coupling effect, the inductances in the d-q frame are denoted as (11) and (12) [24].

TABLE III
TORQUE COMPONENTS CONTRIBUTED BY CURRENT AND INDUCTANCE HARMONICS IN STATIONARY FRAME

k \ (j_1, j_2)	(1,1)	(1, -5) and (-5, 1)	(1, 7) and (7, 1)	(-5, -5)	(-5, 7) and (7, -5)	(7, 7)
0	Zero Instantaneous Torque					
2	**[0th, 16.3 Nm]**	**[6th, 3.1 Nm]**	**[6th, 1.3 Nm]**	[12th, 0.1 Nm]	[0th, 0.1 Nm]	[12th, 0 Nm]
4	**[6th, 1.9 Nm]**	[0th, 0.2 Nm]	[12th, 0.1 Nm]	[6th, 0 Nm]	[6th, 0 Nm]	[18th, 0 Nm]
6	**[6th, 4.7 Nm]**	[0th, -0.2 Nm] [12th, 0.3 Nm]	[0th, 0 Nm] [12th, 0.1 Nm]	[6th, 0 Nm]	[6th, 0 Nm] [18th, 0 Nm]	[6th, 0 Nm]
8	**[6th, 2.9 Nm]**	[12th, 0.4 Nm]	[0th, -0.1 Nm]	[18th, 0 Nm]	[6th, 0 Nm]	[6th, 0 Nm]

$$\mathbf{L_{dq}} = \begin{bmatrix} L_d & M_{dq} \\ M_{qd} & L_q \end{bmatrix} \tag{11}$$

$$\begin{cases} L_d = \sum_{n=0,1,2\cdots} L_{d_n} \cos\left(n\theta_e + \theta_{d_n}\right) \\ L_q = \sum_{n=0,1,2\cdots} L_{q_n} \cos\left(n\theta_e + \theta_{q_n}\right) \\ M_{dq} = M_{qd} = \sum_{n=0,1,2\cdots} M_{dq_n} \cos\left(n\theta_e + \theta_{dq_n}\right) \end{cases} \tag{12}$$

In the *d*-*q* frame, the stored energy in the armature winding can be expressed as

$$W_{co} = \frac{3}{2}\left(\frac{1}{2}\mathbf{I_{dq}}^T \mathbf{L_{dq}} \mathbf{I_{dq}}\right) \tag{13}$$

Based on the co-energy variation at different rotor positions, the instantaneous torque of the SynRM can be derived as

$$T_e = \frac{\partial W_{co}}{\partial \theta_m}\Big|_{i=constant} \tag{14}$$

Combining Eq.(10) ~ Eq.(14), the electromagnetic torque of the SynRM can be solved as

$$T_e = \sum_{\nu_1=6i_1} \sum_{\nu_2=6i_2} \sum_{n=0,1,2\cdots} \frac{3}{4} p I_{\nu 1} I_{\nu 2} \times \begin{Bmatrix} \left(L_d - L_q + \frac{\partial M_{dq}}{\partial \theta_e}\right) \sin\left[\left(\nu_1+\nu_2\right)\theta_e + \beta_{\nu 1} + \beta_{\nu 2}\right] + \\ \left(\frac{\partial L_d - \partial L_q}{2\partial \theta_e} - 2M_{dq}\right) \cos\left[\left(\nu_1+\nu_2\right)\theta_e + \beta_{\nu 1} + \beta_{\nu 1}\right] + \\ \frac{\partial L_d + \partial L_q}{2\partial \theta_e} \cos\left[\left(\nu_1-\nu_2\right)\theta_e + \beta_{\nu 1} - \beta_{\nu 1}\right] \end{Bmatrix} \tag{15}$$

It can be observed from Eq.(15) that the reluctance torque is proportional to the inductance and square of current amplitude. Furthermore, the harmonic orders of the instantaneous torque regarding different rotor positions contain $n+\nu_1+\nu_2$, $n-\nu_1-\nu_2$, $n-\nu_1+\nu_2$, $n+\nu_1-\nu_2$. The harmonic order of 0 is the effective average torque, whereas the higher order harmonic is the adverse pulsating torque.

Similarly, the *d*-*q* axis inductances under sine-wave and square-wave drives can be obtained with the frozen permeability calculation in 2D-FEM, as shown in Fig. 15. Under sine-wave drive, the *d*-*q* axis inductances are almost constant. Since the *d*-axis inductance is strongly determined by the armature current, see Fig. 4, significant 6th order harmonic is introduced in the *d*-axis self-inductance under square-wave drive.

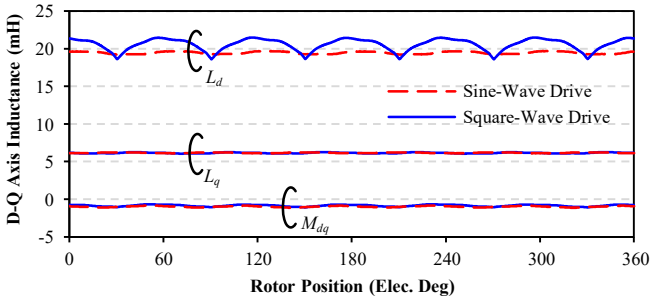

(a)

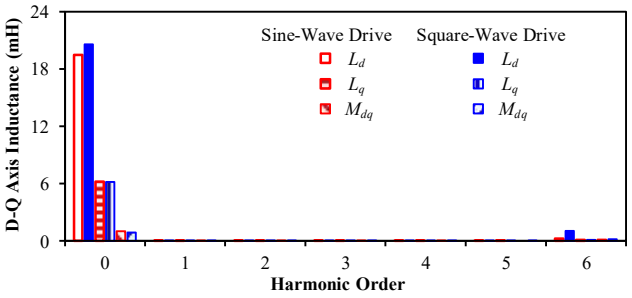

(b)

Fig. 15. *d*-*q* axis inductances obtained from frozen permeability with sine-wave and square-wave drives. (a) Waveforms. (b) Spectra.

In the sine-wave drive, the armature current is ideally sinusoidal without harmonics, therefore, both the *d*-axis current and *q*-axis current are constant, viz. $\nu_1=\nu_2=0$. Considering the constant *d*-*q* axis currents and *d*-*q* axis inductances, the electromagnetic torque of the SynRM can be simplified as Eq.(16) from Eq.(15). The cross-coupling effect and mutual inductance are taken into consideration to accurately predict the instantaneous torque. The existence of mutual inductance tends to cause average torque reduction, and the cross-coupling effect should be suppressed in the SynRM. Overall, the torque is nearly constant concerning the most dominant harmonic, and the torque ripple is negligible. By substituting the current and inductance into Eq.(16), the average torque under ideally sine-wave drive is calculated as 17.2 Nm, which is again consistent with the result of FEA.

$$T_{sin} = \frac{3}{4} p I_m^{\,2} \left[\left(L_d - L_q\right)\sin\left(2\alpha_0\right) - 2M_{dq}\cos\left(2\alpha_0\right)\right] \tag{16}$$

For the square-wave drive, the *d*-*q* axis currents are not constant in the square-wave drive, being abundant with the 6th order harmonic in Fig. 14. Furthermore, the *q*-axis inductance is almost constant once the flux bridges are saturated. However, the *d*-axis inductance is sensitive with the *d*-axis current and saturation level of iron segment. Therefore, the *d*-axis inductance fluctuates with the *d*-axis current, and the 6th order harmonic is observed in the *d*-axis inductance, in consistent with the *d*-axis current variation. Whilst, the *q*-axis inductance hardly varies, as shown in Fig. 15. The harmonics in the *d*-*q* axis currents and inductances will cause certain pulsating torque components, as listed in Table IV. Note, in Table 4, ν_1 and ν_2 are the current harmonic orders, and *n* is the inductance harmonic order.

It can be observed from Table IV that the instantaneous torque with the square-wave drive is mainly composed of the constant value with order of 0th and pulsating torque with order of 6th. The constant torque is produced from the interaction between 0th *d*-*q* axis current and 0th *d*-*q* axis inductances, which is the case for the ideally sine-wave drive. The 6th order pulsating torque mainly has two resources. One is the interaction between the constant *d*-*q* axis currents of 0th with the harmonics in the *d*-*q* axis inductances of 6th. The other is the interaction between the harmonics in the *d*-*q* axis currents of 6th with the 0th *d*-*q* axis inductances. However, it should be noted that the inductances are of negligible harmonics with ideally sine-wave current excitation, whereas additional harmonics are introduced to the inductance due to the current harmonics

caused magnetic saturation. Subsequently, the significant torque ripple can be accounted for the interaction between the current time harmonics and the current-caused inductance harmonics.

TABLE IV
TORQUE COMPONENTS CONTRIBUTED BY CURRENT AND INDUCTANCE HARMONICS IN ROTATING FRAME

n \ (ν_1, ν_2)	(0, 0)	(0, 6) and (6, 0)	(6, 6)
0	**[0th, 16.4 Nm]**	**[6th, 3.7 Nm]**	[0th, 0.2 Nm] [12th, 0.2 Nm]
6	**[6th, 3.1 Nm]**	[0th, -0.1 Nm] [12th, 0.4 Nm]	[6th, 0 Nm] [18th, 0 Nm]

To conclude, the influence of current harmonics on the torque density is acceptable with the substitution of square-wave drive for the original sine-wave drive for low cost application. However, the additional harmonics in the armature current tend to cause local magnetic saturation and harmonics are introduced in the inductance. As a result, although the current harmonics are not abundant, the torque ripple is deteriorated significantly as the interaction between current harmonics with inductance harmonics.

V. CONCLUSION

In this paper, square-wave drive is utilized for the SynRM to reduce the cost of hardware and to simplify the control strategy. Since the inductance is relatively large in the SynRM, the harmonics in the current are not really abundant even with the square-wave drive. By replacing the conventional sine-wave drive with the square-wave drive, similar performances are achieved concerning the torque density and voltage utilization, except that the torque ripple becomes much higher. Therefore, the square-wave drive for SynRM is still promising for some low-cost applications, in which the torque ripple is not critically concerned.

Although the current time harmonics are not abundant in the square-wave drive, the torque ripple remarkably increases and the dominant pulsating torque is the 6th-order harmonic. To investigate the origination of the additional torque pulsation, both the a-b-c phase inductance model and *d-q* axis inductance model are established to calculate the certain torque components. It is found that the current time harmonics have a detrimental effect on the flux density harmonics, and consequently, on the undesirable inductance variations. The dominant 6th torque pulsation comes from the interaction between the current harmonics and the inductance fundamental as well as that between the current fundamental and the inductance high order harmonics. Due to the local saturation, even low-level current time harmonics tend to cause remarkable inductance harmonics, and therefore, the significant torque pulsation.

REFERENCES

[1] T. Matsuo and T. A. Lipo, "Rotor design optimization of synchronous reluctance machine," *IEEE Trans. Energy Convers.*, vol. 9, no. 2, pp. 359-365, Jun 1994.

[2] K. T. Chau, C. C. Chan and C. Liu, "Overview of permanent-magnet brushless drives for electric and hybrid electric vehicles," *IEEE Trans. Ind. Electron.*, vol. 55, no. 6, pp. 2246-2257, June 2008.

[3] A. Vagati, "The synchronous reluctance solution: a new alternative in AC drives," *Industrial Electronics, Control and Instrumentation, 1994. IECON '94., 20th International Conference on*, Bologna, 1994, pp. 1-13.

[4] T. M. Jahns and W. L. Soong, "Pulsating torque minimization techniques for permanent magnet AC motor drives-a review," *IEEE Trans. Ind. Electron.*, vol. 43, no. 2, pp. 321-330, Apr 1996.

[5] S. Cai, M. J. Jin, H. Hao, and J. X. Shen, "Comparative study on synchronous reluctance and PM machines," *COMPEL: The International Journal for Computation and Mathematics in Electrical and Electronic Engineering,* vol. 35, pp. 607-623, 2016.

[6] A. Boglietti, A. Cavagnino, M. Pastorelli and A. Vagati, "Experimental comparison of induction and synchronous reluctance motors performance," *Fourtieth IAS Annual Meeting. Conference Record of the 2005 Industry Applications Conference, 2005.*, 2005, pp. 474-479 Vol. 1.

[7] J. X. Shen, S. Cai, H. Hao and M. J. Jin, "Investigation on torque ripple of synchronous reluctance machine with square-wave drive," *2017 20th International Conference on Electrical Machines and Systems (ICEMS)*, Sydney, NSW, 2017, pp. 1-9.

[8] M. Ferrari, N. Bianchi and E. Fornasiero, "Analysis of Rotor Saturation in Synchronous Reluctance and PM-Assisted Reluctance Motors," *IEEE Trans. Ind. Appl.*, vol. 51, no. 1, pp. 169-177, Jan.-Feb. 2015.

[9] M. Gamba, G. Pellegrino and A. Vagati, "A new PM-assisted Synchronous Reluctance machine with a nonconventional fractional slot per pole combination," *2014 International Conference on Optimization of Electrical and Electronic Equipment (OPTIM)*, Bran, 2014, pp. 268-275.

[10] J. B. Wang, V. I. Patel and W. Wang, "Fractional-Slot Permanent Magnet Brushless Machines with Low Space Harmonic Contents," *IEEE Trans. Magn.*, vol. 50, no. 1, pp. 1-9, Jan. 2014.

[11] G. Pellegrino, P. Guglielmi, A. Vagati and F. Villata, "Core Losses and Torque Ripple in IPM Machines: Dedicated Modeling and Design Tradeoff," *IEEE Trans. Ind. Appl.*, vol. 46, no. 6, pp. 2381-2391, Nov.-Dec. 2010.

[12] A. Vagati, M. Pastorelli, G. Francheschini and S. C. Petrache, "Design of low-torque-ripple synchronous reluctance motors," *IEEE Trans. Ind. Appl.*, vol. 34, no. 4, pp. 758-765, Jul/Aug 1998.

[13] R. R. Moghaddam, F. Magnussen and C. Sadarangani, "Novel rotor design optimization of Synchronous Reluctance Machine for low torque ripple," *2012 XXth International Conference on Electrical Machines*, Marseille, 2012, pp. 720-724.

[14] M. Obata, S. Morimoto, M. Sanada and Y. Inoue, "Performance of PMASynRM With Ferrite Magnets for EV/HEV Applications Considering Productivity," *IEEE Trans. Ind. Appl.*, vol. 50, no. 4, pp. 2427-2435, July-Aug. 2014.

[15] N. Bianchi, S. Bolognani, D. Bon and M. Dai Pre, "Rotor Flux-Barrier Design for Torque Ripple Reduction in Synchronous Reluctance and PM-Assisted Synchronous Reluctance Motors," *IEEE Trans. Ind. Appl.*, vol. 45, no. 3, pp. 921-928, May-june 2009.

[16] N. Bianchi, S. Bolognani, D. Bon and M. Dai PrÉ, "Torque Harmonic Compensation in a Synchronous Reluctance Motor," *IEEE Trans. Energy Convers.*, vol. 23, no. 2, pp. 466-473, June 2008.

[17] M. Sanada, K. Hiramoto, S. Morimoto and Y. Takeda, "Torque ripple improvement for synchronous reluctance motor using an asymmetric flux barrier arrangement," *IEEE Trans. Ind. Appl.*, vol. 40, no. 4, pp. 1076-1082, July-Aug. 2004.

[18] K. Wang, Z. Q. Zhu, G. Ombach, M. Koch, S. Zhang, and J. Xu, "Torque ripple reduction of synchronous reluctance machines: using asymmetric flux-barrier," *COMPEL: The International Journal for Computation and Mathematics in Electrical and Electronic Engineering,* vol. 34, pp. 18-31, 2015.

[19] Y. Q. Lin, Y. Sun, Y. C. Wang, S. Cai, and J. X. Shen, Radial electromagnetic force and vibration in synchronous reluctance motors with asymmetric rotor structures, IET Electric Power Applications, Vol. 15, No. 9, September 2021, pp. 1125-1137,

[20] J. X. Shen, S. Cai, H. Hao and M. J. Jin, "Comprehensive parameter design for transversally laminated synchronous reluctance machines," *2016 19th International Conference on Electrical Machines and Systems (ICEMS)*, Chiba, 2016, pp. 1-9.

[21] M. Bertoluzzo, G. Buja, R. K. Keshri and R. Menis, "Sinusoidal versus square-wave current supply of pm brushless dc drives: a convenience analysis," *IEEE Trans. Ind. Electron.*, vol. 62, no. 12, pp. 7339-7349, Dec. 2015.

[22] M. S. Islam, S. Mir, T. Sebastian and S. Underwood, "Design considerations of sinusoidally excited permanent magnet machines for low torque ripple applications," *Conference Record of the 2004 IEEE Industry Applications Conference, 2004. 39th IAS Annual Meeting.*, Seattle, WA, USA, 2004, pp. 1723-1730.

[23] J. X. Shen, D. Shi, C. F. Wang, P. Li, K. Wang, and M. J. Jin, "Torque ripple analysis for IPM AC motors," *COMPEL: The International Journal for Computation and Mathematics in Electrical and Electronic Engineering,* vol. 33, pp. 1514-1526, 2014.

[24] A. Fratta, G. P. Troglia, A. Vagati and F. Villata, "Evaluation of torque ripple in high performance synchronous reluctance machines," *Conference Record of the 1993 IEEE Industry Applications Conference Twenty-Eighth IAS Annual Meeting*, Toronto, 1993, pp. 163-170.

Jian-Xin Shen received the B.S. and M.S. degrees from Xi'an Jiaotong University, China, in 1991 and 1994. He received the Ph.D. degrees from Zhejiang University, China, in 1997. From 1997 to 1999, he studied as a postdoctoral fellow at Nanyang Technological University, Singapore. From 1999 to 2002, He was an Associate Researcher (meanwhile working towards a second PhD degree, the degree awarded in July 2003) at Sheffield University, UK. From 2002 to 2004, he was a Research Engineer with IMRA Europe SAS, UK Research Centre, UK, a research centre associated with Aisin Seiki, Japan. Since 2004, he has been a professor at Zhejiang University, China. He has published over 270 technical papers on journals or conferences and received 9 international paper awards. He holds over 40 awarded patents. Jian-Xin Shen has been a senior member of IEEE since 2002 and a senior member of CES since 2009. Since 2014, he has been a fellow of IET.

His current research interests include electrical machine topologies, motor drives, motion control, applications, etc.

Shun Cai was born in Hubei, China in 1993. He received the B.Eng. and M.Sc. degrees from Zhejiang University, Hangzhou, China, in 2014 and 2017, respectively and the Ph.D. degree from the University of Sheffield, Sheffield, U.K., in 2020, all in electrical engineering.

Since 2021, He has been a Research Fellow with Nanyang Technological University, Singapore. His research interests include design and analysis of novel permanent magnet machines for automobile application and renewable power generation.

Dong-Min Miao was was born in Hangzhou, China, in 1988. She received the B.Eng. degree from Zhejiang University, Hangzhou, China, in 2011, and the double Ph. D. degrees from Zhejiang University and Université Libre de Bruxelles, Brussels, Belgium, in 2016, all in electrical engineering. Her main research interests include the PM machine design and different motor/generator control strategies.

Dan Shi was born in Luoyang, China, in 1986. She received the B.SC. and M.SC. degrees in Electrical Engineering at Zhejiang University Hangzhou, China, in 2009 and 2012 respectively, and the Ph.D degree in Robotics Control and Intelligent Systems in École polytechnique fédérale de Lausanne (EPFL), Switzerland, in 2016. She is currently working as a postdoc in Department of Electrical Engineering in Zhejiang University. Her research interests include research and applications in high speed permanent magnet machines.

Jacek F. Gieras received the M.Eng. degree (with distinction) from the Technical University of Lodz, Lodz, Poland, in 1971, and the Ph.D. degree in electrical engineering (electrical machines) and the Dr. Habil. degree (corresponding to the D.Sc. degree) in electrical engineering from Poznan University of Technology, Poznan, Poland, in 1975 and 1980, respectively.

In 1987, he was promoted to the rank of Full Professor (a life title given by the President of the Republic of Poland). Since 1998, he has been with United Technologies Corporation, Hartford, CT, where, most recently, he has been with Hamilton Sundstrand Applied Research. Since 2007, he has been a Faculty Member (Full Professor) in the Department of Electrical Engineering, University of Technology and Life Sciences, Bydgoszcz, Poland. He has authored or coauthored 11 books and over 250 scientific and technical papers and is the holder of 70 U.S. patents and patent publications. His most important books are *Linear Induction Drives* (Oxford University Press, 1994), *Permanent Magnet Motor Technology: Design and Applications* (Marcel Dekker Inc., 1996; Marcel Dekker Inc., 2002; and Taylor & Francis, 2010), *Linear Synchronous Motors: Transportation and Automation Systems* (CRC Press, 1999 and 2011), *Axial Flux Permanent Magnet Brushless Machines* (Springer–Kluwer Academic, 2004 and 2008) (with coauthors R.Wang and M. J. Kamper), *Noise of Polyphase Electric Motors* (CRC Press–Taylor & Francis, 2005) (with coauthors C. Wang and J. C. Lai), and *Advancements in Electric Machines* (Springer, 2008). His research areas include electrical machines, drives, electromagnetics, power systems, and railway engineering.

Prof. Gieras is a Hamilton Sundstrand Fellow (United Technologies Corporation), a full member of the International Academy of Electrical Engineering, and a member of the steering committees of numerous international conferences.

Yun-Chong Wang was born in Liaoning, China, in 1987. He received the B.S. and M.S. degrees from Zhejiang University, Zhejiang, China, in 2010 and 2013, respectively, and Ph.D. degree from the Hong Kong Polytechnic University, Hong Kong ， in 2017, all in electrical engineering. Since 2020, he has been an Associate Professor of Electrical Engineering with Zhejiang University. He has authored more than 30 technical papers. His research interests include the design and control of permanent magnet machines, novel electrical motors for electrical vehicles, hybrid electrical vehicles and renewable energy conversion system.